

# Neutron star tidal disruption in mixed binaries: the imprint of the equation of state

V. Ferrari<sup>1</sup>, L. Gualtieri<sup>1</sup>, F. Pannarale<sup>1,2</sup>

<sup>1</sup>*Dipartimento di Fisica, “Sapienza” Università di Roma & Sezione INFN Roma1, Piazzale Aldo Moro 5, 00185, Roma, Italy*

<sup>2</sup>*Max-Planck-Institut für Gravitationsphysik, Albert-Einstein-Institut, Potsdam-Golm, Germany*

We study the tidal disruption of neutron stars in black hole-neutron star coalescing binaries. We calculate the critical orbital separation at which the star is disrupted by the black hole tidal field for several equations of state describing the matter inside the neutron star, and for a large set of the binary parameters. When the disruption occurs before the star reaches the innermost stable circular orbit, the gravitational wave signal emitted by the system is expected to exhibit a cutoff frequency  $\nu_{GWtide}$ , which is a distinctive feature of the waveform. We evaluate  $\nu_{GWtide}$  and show that, if this frequency will be found in a detected gravitational wave, it will allow one to determine the neutron star radius with an error of a few percent, providing valuable information on the behaviour of matter in the stellar core.

PACS numbers: 04.30.-w, 04.25.dk, 26.60.Kp

## I. INTRODUCTION

The coalescence of neutron star-neutron star (NS-NS) and black hole-neutron star (BH-NS) binaries is one of the most promising sources of gravitational waves to be detected by ground based gravitational wave detectors like Virgo and LIGO [1]. These detectors have now reached the planned sensitivity and they will evolve toward a second generation, the advanced (Virgo and LIGO) detectors, with a sensitivity enhanced by an order of magnitude. Furthermore, a design study for an even more sensitive third generation detector, ET (Einstein Telescope), is in progress [2].

In a recent study, based on a population synthesis approach [3], the formation and the evolution of compact binary systems has been followed from the onset of star formation, both in the Galactic field, where their massive binary progenitors evolve in isolation, and in dense clusters, where they can form at high rates due to dynamical interactions. The authors estimate that advanced LIGO should detect the merger of NS-NS binaries at a rate of  $\sim 15$  events per year and the merger of BH-NS binaries at a rate of  $\sim 1$  per year. Similar estimates hold for the advanced version of Virgo. Thus, it is reasonable to expect that in a near future we may be able to detect the gravitational wave (GW) signals emitted by these sources and study their features.

A further reason to be interested in these coalescing binaries is that they have been proposed as providing the engine for short gamma-ray bursts (SGRBs); the detection of a gravitational wave signal emitted by one of these systems in coincidence with a SGRB would validate this model, thus clarifying one of the most interesting open issues in astrophysics.

In this paper we study the disruption of a neutron star in a BH-NS coalescing binary, to envisage a method to extract information on the equation of state (EOS) of matter in the NS interior from the detection of the gravitational wave signal emitted in the process. We use the

*affine model* approach [4],[5],[6],[7], which treats the NS as an extended object, which responds to its self-gravity, to its internal pressure forces and to the relativistic BH tidal field, under the constraint that its shape is always that of an ellipsoid. In the original formulation of this model, the internal structure of the star was treated at a Newtonian level and the EOS was assumed to be polytropic. In [8] (to be referred to as Paper I hereafter) we have improved this approach by introducing a general relativistic description of the stellar structure, and generalizing the relevant equations to include more general equations of state. This improved approach has been applied to study quasi-equilibrium sequences of BH-NS binaries, and to determine the critical orbital separation at which the star is torn apart by the black hole tidal field.

When the NS is disrupted before reaching the Innermost Stable Circular Orbit (ISCO), the emitted GW signal is expected to change abruptly and its amplitude is expected to decrease sharply; such signal should exhibit a cutoff frequency  $\nu_{GWtide}$ , corresponding to the orbit at which the disruption occurs, i.e.  $\nu_{GWtide} = 2\nu_{orb tide}$ . This prediction is confirmed by numerical simulations where the coalescence of a black hole and a neutron star and the tidal disruption of the star have been studied i) in the framework of Newtonian gravity [9], [10], and ii) in full general relativity [11], [12].

The frequency cutoff is a distinctive feature of the waveform emitted by a BH-NS coalescing binary and indicates the disruption of the star. This was first pointed out in [13], where a relation between  $\nu_{GWtide}$  and the stellar radius was derived, using the formulation of the affine model appearing in [14] and describing the inspiralling of an incompressible, homogeneous, Newtonian ellipsoid moving on circular orbits around a rotating black hole. Hints on the role of the compressibility were derived in [13] using some results of [6], where the same process was studied for a polytropic, Newtonian star.

In this paper we study the relation between the cutoff frequency and the neutron star EOS. Using the same ap-

proach developed in Paper I, we explicitly compute for which values of the masses of the binary components and of the black hole angular momentum the star is tidally disrupted before reaching the ISCO, for a variety of realistic equations of state. Knowing the disruption distance  $r_{tide}$ , we evaluate  $\nu_{GWtide}$  and show how a measure of this quantity from a detected GW signal may be used to infer interesting information on the equation of state of matter in the neutron star interior.

It is known that the fully relativistic numerical study of the last phases of BH-NS binary coalescence is a quite difficult task, especially for large values of the mass ratio  $q = M_{BH}/M_{NS}$ ; this is due to a number of reasons, which include the lack of symmetry, the difficulty in evolving the NS while handling the BH singularity, and the prohibitively high computational costs required to span the parameter space (mass ratio, EOS, spins etc.). For these reasons, the literature on the subject is limited to a restricted number of studies, most of which are in the framework of Newtonian gravity. BH-NS coalescence in general relativity has been studied in the following papers (see [15] for a recent review on the subject): non spinning black hole and  $M_{BH} \gg M_{NS}$  in [16];  $q = 10$  in [17];  $q = 1, 3, 5$  in [11]; and  $M_{BH} = 3.2M_{\odot}$ ,  $M_{BH} = 4M_{\odot}$  and  $M_{NS} = 1.4M_{\odot}$  in [18]. In [19], quasi-equilibrium sequences of black hole-neutron star binaries have been studied in general relativity for  $q = 1, 2, 3, 5, 10$ . The case of a rotating black hole has been considered in [11], where the coalescence has been studied for three values of the black hole angular momentum ( $a/M_{BH} = -0.5, 0, 0.75$ ) and for  $q = 3$ , whereas in [12] the case  $q = 10$  has been investigated. It should be stressed that in *all* these studies the neutron star is modeled using a polytropic equation of state.

The improved affine model approach which we use in our study is an approximate method, but it has the advantage of allowing one to explore a large region of the parameter space, including large values of the mass ratio  $q = M_{BH}/M_{NS}$ , and to use modern equations of state to model matter in the neutron star interior, at a much lower computational cost than fully relativistic simulations.

With respect to ref. [13] our study introduces several novelties: we describe the internal structure of the star using general relativity, we explicitly take into account the stellar compressibility and describe the matter inside the star using realistic equations of state; in addition, in [13]  $\nu_{GWtide}$  was provided by the Kerr geometry in the approximation of a point mass NS following geodesics in this geometry, while we determine this quantity using the 2.5 Post Newtonian equations of motion for the orbital dynamics of a binary system.

The plan of the paper is the following. In Section II we briefly describe the affine approach; in Section III we discuss how to determine the cutoff frequency  $\nu_{GWtide}$ . The equations of state we employ are briefly described in Section IV; in Section V we discuss the errors which affect the measure of the binary parameters from a de-

tected GW signal, and how they propagate and affect the evaluation of  $\nu_{GWtide}$  and of the neutron star radius. The results of our study are reported in Section VI and in Section VII we draw our conclusions.

## II. THE IMPROVED AFFINE MODEL EQUATIONS

The equations of the improved affine model approach, which we need in order to determine the radial distance  $r_{tide}$  at which the neutron star is torn apart by the tidal interaction with the black hole, are described in detail in Paper I. Here we will summarise the assumptions underlying this approach and we shall write only the equations to be solved.

### 1. Relevant assumptions and equations

We consider a star in the tidal field of a Kerr BH whose center of mass follows equatorial, circular orbits; while moving, the star maintains an ellipsoidal shape; more precisely it is a Riemann-S type ellipsoid, i.e. its spin and vorticity are parallel and their ratio is constant (see [20]). The NS equilibrium structure is determined using the stellar structure equations of General Relativity, while dynamical behaviour is governed by Newtonian hydrodynamics improved by the use of an effective relativistic self-gravity potential. The equations for the NS deformations are written in the principal frame, i.e. the frame associated with the principal axes of the stellar ellipsoid. Tidal effects on the orbital motion are neglected, as well as the perturbation that the star induces on the BH.

We study the evolution of the system in the quasi-equilibrium approximation, i.e. we neglect all time derivatives appearing in the ordinary differential equations of the model. Physically this means that we assume that the NS follows a quasi-equilibrium sequence during the BH-NS coalescence; according to the model, moreover, the circulation  $\mathcal{C}$  of the fluid along this sequence is constant. In particular, we set  $\mathcal{C} = 0$ , that is, we consider the NS fluid to be irrotational. In the principal frame, the fluid variables of the improved affine model are five: the three principal axes of the stellar ellipsoid  $a_1, a_2$  and  $a_3$ , the angular frequency of the internal fluid motion  $\Lambda$  and the star spin  $\Omega$ . The axes  $a_1$  and  $a_2$  both belong to the orbital plane, while  $a_3$  is perpendicular to it;  $a_1$  indicates the axis that lies along the binary orbital radius. The quasi-equilibrium equations governing these variables are:

$$\begin{aligned} 0 &= a_1(\Lambda^2 + \Omega^2) - 2a_2\Lambda\Omega \\ &+ \frac{1}{2} \frac{\widehat{V}}{\mathcal{M}} R_{NS}^3 a_1 \tilde{A}_1 + \frac{R_{NS}^2}{\mathcal{M}} \frac{\Pi}{a_1} - c_{11} a_1 \\ 0 &= a_2(\Lambda^2 + \Omega^2) - 2a_1\Lambda\Omega \end{aligned} \quad (1)$$

$$+ \frac{1}{2} \frac{\widehat{V}}{\widehat{\mathcal{M}}} R_{NS}^3 a_2 \tilde{A}_2 + \frac{R_{NS}^2}{\widehat{\mathcal{M}}} \frac{\Pi}{a_2} - c_{22} a_2 \quad (2)$$

$$0 = \frac{1}{2} \frac{\widehat{V}}{\widehat{\mathcal{M}}} R_{NS}^3 a_3 \tilde{A}_3 + \frac{R_{NS}^2}{\widehat{\mathcal{M}}} \frac{\Pi}{a_3} - c_{33} a_3 \quad (3)$$

$$\phi = \Psi \quad (4)$$

where  $\widehat{V}$  and  $\widehat{\mathcal{M}}$  are, respectively, the effective relativistic self-gravity potential and the scalar quadrupole moment of the NS at spherical equilibrium (see below).  $R_{NS}$  is the NS radius and the  $\tilde{A}_i$ 's are defined as

$$\tilde{A}_i = \int_0^\infty \frac{d\sigma}{(a_i^2 + \sigma) \sqrt{(a_1^2 + \sigma)(a_2^2 + \sigma)(a_3^2 + \sigma)}}. \quad (5)$$

The  $c_{ij}$ 's denote the components of the BH tidal tensor in the principal frame;  $\phi$  — which is connected to  $\Omega$  by  $\dot{\phi} \equiv \Omega$  — is the angle that brings the parallel-propagated frame in the principal frame, by a rotation around the  $a_3$  axis [21]. Finally,  $\Psi$  is an angle that governs the rotation of the parallel-propagated frame in order to preserve its parallel transport, and its time evolution is given by

$$\dot{\Psi} = \sqrt{\frac{M_{BH}}{r^3}}, \quad (6)$$

where  $M_{BH}$  and  $r$  are the BH mass and the BH-NS orbital separation respectively. Notice that the last equation and Eq. (4) imply that

$$\Omega = \sqrt{\frac{M_{BH}}{r^3}}. \quad (7)$$

The fifth equation for the five fluid variables is provided by the definition of the circulation

$$\mathcal{C} = \frac{\widehat{\mathcal{M}}}{R_{NS}^2} [(a_1^2 + a_2^2)\Lambda - 2a_1 a_2 \Omega], \quad (8)$$

so that for irrotational fluids one has

$$\Lambda = \frac{2a_1 a_2 \Omega}{a_1^2 + a_2^2}. \quad (9)$$

The effective relativistic self-gravity potential is given by

$$\widehat{V} = -4\pi \int_0^{R_{NS}} \frac{d\Phi_{TOV}}{d\hat{r}} \hat{r}^3 \hat{\rho} d\hat{r}, \quad (10)$$

where  $d\Phi_{TOV}/d\hat{r}$  is given by the Tolman-Oppenheimer-Volkoff (TOV) stellar structure equations

$$\frac{d\Phi_{TOV}}{dr} = \frac{[\epsilon(r) + P(r)][m_{TOV}(r) + 4\pi r^3 P(r)]}{\rho(r)r[r - 2m_{TOV}(r)]}$$

$$m_{TOV}(r) = 4\pi \int_0^r dr' r'^2 \epsilon(r').$$

The scalar quadrupole moment  $\widehat{\mathcal{M}}$  is defined as

$$\widehat{\mathcal{M}} = \frac{4\pi}{3} \int_0^{R_{NS}} r^4 \rho dr \quad (11)$$

and, like  $\widehat{V}$ , must be calculated at spherical equilibrium. Finally, the relevant Kerr BH tidal tensor components are

$$c_{11} = \frac{M_{BH}}{r^3} \left[ 1 - 3 \frac{r^2 + K}{r^2} \cos^2(\Psi - \phi) \right] \quad (12)$$

$$c_{22} = \frac{M_{BH}}{r^3} \left[ 1 - 3 \frac{r^2 + K}{r^2} \sin^2(\Psi - \phi) \right] \quad (13)$$

$$c_{33} = \frac{M_{BH}}{r^3} \left( 1 + 3 \frac{K}{r^2} \right), \quad (14)$$

where

$$K = (aE - L_z)^2; \quad (15)$$

$a$  is the black hole spin parameter, and  $E$  and  $L_z$  are, respectively, the energy and the  $z$ -orbital angular momentum per unit mass. Since we consider circular equatorial geodesics,  $E$  and  $L_z$  are

$$E = \frac{r^2 - 2M_{BH}r + a\sqrt{M_{BH}r}}{r\sqrt{P}}$$

$$L_z = \frac{\sqrt{M_{BH}r}(r^2 - 2a\sqrt{M_{BH}r} + a^2)}{r\sqrt{P}}, \quad (16)$$

where

$$P = r^2 - 3M_{BH}r + 2a\sqrt{M_{BH}r}. \quad (17)$$

## 2. Numerical integration

We solve Eqs. (1)-(3), with the aid of Eqs.(7), (9) and of definitions (5), (10), (11), (12)-(14), by adopting a multidimensional Newton-Raphson scheme [22] in order to determine the values of the axes of the ellipsoid for each quasi-stationary orbit, identified by the orbital separation  $r$ .

We start by solving the TOV stellar structure equations for a non-rotating spherical neutron star in equilibrium. We then fix the black hole spin parameter  $a$  and the binary mass ratio  $q$  and place the star at a distance  $r_0 \gg R_{NS}$  from the black hole (we obviously make sure that the sequence we obtain is independent of  $r_0$ ). Subsequently, we gradually reduce the orbital separation and solve Eqs.(1)-(3) at each step and monitor the star axes until a critical separation  $r_{tide}$  is reached, at which a quasi-equilibrium configuration is no longer possible. This critical distance physically corresponds to the tidal disruption of the neutron star. It may be identified by exploiting the fact that the Newton-Raphson algorithm cannot find any solution to the system of equations, or by

calculating numerically the derivative  $\partial r_{norm}/\partial(a_2/a_1)$ , where

$$r_{norm} = \frac{r}{R_{NS}} \left( \frac{M_{NS}}{M_{BH}} \right)^{1/3},$$

and keeping track of it since it tends to zero at tidal disruption: both methods yield the same values of  $r_{tide}$ . We mention that an alternative approach to evaluate  $r_{tide}$  in a Newtonian framework, based on the estimate of the Roche lobe radius, has been used in [23]. If the tidal disruption is not encountered, the quasi-equilibrium ends when the neutron star surface crosses the black hole horizon and hence the coalescence terminates with a plunge.

The quantity  $r_{tide}$  has to be compared with the value of the radius of the innermost stable circular orbit  $r_{ISCO}$ , which is determined by using the formulae derived in [24] for a point mass in the gravitational field of a Kerr BH:

$$\begin{aligned} r_{ISCO} &= M_{BH} \{3 + Z_2 \mp [(3 - Z_1)(3 + Z_1 + 2Z_2)]^{1/2}\} \\ Z_1 &= 1 + (1 - a^2/M_{BH}^2)^{1/3} \\ &\quad \times [(1 + a/M_{BH})^{1/3} + (1 - a/M_{BH})^{1/3}] \\ Z_2 &= (3a^2/M_{BH}^2 + Z_1^2)^{1/2}, \end{aligned} \quad (18)$$

where the upper (lower) sign holds for co- (counter-)rotating orbits. We remind the reader that if  $r_{tide} > r_{ISCO}$  the star is disrupted before the merger starts, and the gravitational signal will exhibit a cutoff at a frequency  $\nu_{GWtide}$ .

### III. DETERMINATION OF THE CUTOFF FREQUENCY $\nu_{GWtide}$

To compute  $\nu_{GWtide}$ , we model the inspiral of the mixed binary by means of a post-Newtonian (PN) approach and truncate the inspiral when the orbital separation reaches  $r_{tide}$ ; we then read off the orbital frequency at the tidal disruption  $\nu_{orb\ tide}$ : this is related to the GW frequency by  $\nu_{GWtide} = 2\nu_{orb\ tide}$ .

We follow a Hamiltonian approach. The conservative part of the two-body Hamiltonian is known up to order 3PN, e.g. [25]; however, we shall truncate it at 2PN order since we will use GW dissipation terms of order 2.5PN [26]. The PN-expanded Hamiltonian for the relative motion of the BH-NS binary is

$$\mathcal{H}_{orb}^{Exp} = \mathcal{H}_N + \mathcal{H}_{PN} + \mathcal{H}_{2PN} + \mathcal{H}_{SO} + \mathcal{H}_{SS}, \quad (19)$$

the single contributions being:

$$\begin{aligned} \mathcal{H}_N &= \frac{1}{2\mu} \left( P_r^2 + \frac{P_\varphi^2}{r^2} \right) - \frac{G_N \mu M_{Tot}}{r} \\ \mathcal{H}_{PN} &= \frac{3\eta - 1}{8c^2 \mu^3} \left( P_r^2 + \frac{P_\varphi^2}{r^2} \right)^2 \\ &\quad - \frac{G_N M_{Tot}}{2c^2 \mu r} \left\{ (3 + \eta) \left( P_r^2 + \frac{P_\varphi^2}{r^2} \right) + \eta P_r^2 \right\} \end{aligned} \quad (20)$$

$$+ \frac{G_N^2 \mu M_{Tot}^2}{2c^2 r^2} \quad (21)$$

$$\begin{aligned} \mathcal{H}_{2PN} &= \frac{1 - 5\eta + 5\eta^2}{16c^4 \mu^5} \left( P_r^2 + \frac{P_\varphi^2}{r^2} \right)^3 \\ &\quad + \frac{G_N M_{Tot}}{8c^4 \mu^3 r} \left[ (5 - 20\eta - 3\eta^2) \left( P_r^2 + \frac{P_\varphi^2}{r^2} \right)^2 \right. \\ &\quad \left. - 2\eta^2 P_r^2 \left( P_r^2 + \frac{P_\varphi^2}{r^2} \right) - 3\eta^2 P_r^4 \right] \\ &\quad + \frac{G_N^2 M_{Tot}^2}{2c^4 \mu r^2} \left[ (5 + 8\eta) \left( P_r^2 + \frac{P_\varphi^2}{r^2} \right) + 3\eta P_r^2 \right] \\ &\quad - \frac{G_N^3 (1 + 3\eta) \mu M_{Tot}^3}{4c^4 r^3} \end{aligned} \quad (22)$$

$$\mathcal{H}_{SO} = \frac{G_N}{c^2 r^3} \mathbf{L} \cdot \left( 2 + \frac{3M_{NS}}{2M_{BH}} \right) \mathbf{J}_{BH} \quad (23)$$

$$\begin{aligned} \mathcal{H}_{SS} &= \frac{G_N}{c^2 r^3} [3(\mathbf{J}_{BH} \cdot \mathbf{n})(\mathbf{J}_{BH} \cdot \mathbf{n}) \\ &\quad - (\mathbf{J}_{BH} \cdot \mathbf{J}_{BH})] \frac{M_{NS}}{M_{BH}} \end{aligned} \quad (24)$$

where  $G_N$  is the gravitational constant,  $c$  is the speed of light,  $M_{Tot} = M_{BH} + M_{NS}$  is the total mass of the system,  $\mu = M_{BH} M_{NS} / M_{Tot}$  is its reduced mass,  $\eta = \mu / M_{Tot}$  is the symmetric mass ratio,  $P_r$  and  $P_\varphi$  are the conjugate variables of the orbital separation  $r$  and the orbit angle coordinate  $\varphi$ ,  $\mathbf{L} = \mathbf{r} \times \mathbf{P}$  is the orbital angular momentum and  $\mathbf{J}_{BH}$  is the spin angular momentum of the black hole. The vectors  $\mathbf{L}$  and  $\mathbf{J}_{BH}$  are both perpendicular to the orbit plane; the magnitude of the latter is equal to  $aM_{BH}$  and such vector is not evolved as a dynamic variable in order to follow the spirit of the affine model, according to which the presence of the NS does not influence the BH. The spin-orbit (SO) and spin-spin (SS) contributions to  $\mathcal{H}_{orb}^{Exp}$  therefore reduce to

$$\mathcal{H}_{SO} = \frac{G_N}{c^2 r^2} \sqrt{P_r^2 + \frac{P_\varphi^2}{r^2}} \left( 2 + \frac{3M_{NS}}{2M_{BH}} \right) J_{BH} \quad (25)$$

and

$$\mathcal{H}_{SS} = \frac{2G_N}{c^2 r^3} \frac{M_{NS}}{M_{BH}} J_{BH}^2. \quad (26)$$

The dynamics described by this Hamiltonian is supplied with GW dissipation by means of the 2.5PN non-conservative terms

$$f_r = -\frac{8G_N^2}{15c^5 \eta r^2} \left( 2P_r^2 + \frac{6P_\varphi^2}{r^2} \right) \quad (27)$$

$$f_\varphi = -\frac{8G_N^2}{3c^5} \frac{P_r P_\varphi}{\eta r^4} \quad (28)$$

$$F_r = -\frac{8G_N^2}{3c^5} \frac{P_r}{r^4} \left( \frac{P_\varphi^2}{\eta r} - \frac{G_N \eta M_{Tot}^3}{5} \right) \quad (29)$$

$$F_\varphi = -\frac{8G_N^2}{5c^5} \frac{P_\varphi}{\eta r^3} \left( \frac{2G_N \eta^2 M_{Tot}^3}{r} + \frac{2P_\varphi^2}{r^2} - P_r^2 \right) \quad (30)$$

to be included in the Hamilton equations of motion as

$$\frac{dr}{dt} = \frac{\partial \mathcal{H}}{\partial P_r} + f_r \quad (31)$$

$$\frac{d\varphi}{dt} = \frac{\partial \mathcal{H}}{\partial P_\varphi} + f_\varphi \quad (32)$$

$$\frac{dP_r}{dt} = -\frac{\partial \mathcal{H}}{\partial r} + F_r \quad (33)$$

$$\frac{dP_\varphi}{dt} = -\frac{\partial \mathcal{H}}{\partial \varphi} + F_\varphi. \quad (34)$$

Within this Hamiltonian approach, once the binary orbit is evolved until  $r = r_{tide}$ , the GW cutoff frequency due to the NS tidal disruption  $\nu_{GWtide}$  is given by

$$\nu_{GWtide} \equiv 2\nu_{orb\ tide} = \frac{P_\varphi}{\pi \mu r^2} \Big|_{r_{tide}}. \quad (35)$$

#### IV. EQUATIONS OF STATE

The equation of state of matter at densities larger than the saturation density of nuclear matter,  $\rho_0 = 2.67 \cdot 10^{14}$  g/cm<sup>3</sup>, is uncertain. At these densities, which are typical of a neutron star core, neutrons can no longer be considered as non interacting particles, and different ways of modeling their interactions lead to a different composition, which may include heavy baryons, quarks etc.. All available EOSs of strongly interacting matter have been obtained within models based on the theoretical knowledge of the underlying dynamics and constrained, as much as possible, by empirical data. Modern EOSs are derived within two main, different approaches: non-relativistic nuclear many-body theory (NMBT) and relativistic mean field theory (RMFT). As representative of NMBT we choose two EOSs named APR2 and BBS1. For APR2 matter consists of neutrons, protons, electrons and muons ( $n, p, e, \mu$ ) in weak equilibrium. The Hamiltonian includes two- and three- nucleon interaction terms; the two-nucleon term is the Argonne  $v_{18}$  potential [27], the three-nucleon term is the Urbana IX potential [28]. The many-body Schrödinger equation is solved using a variational approach [29, 30]. The calculations include relativistic corrections to the two-nucleon potential, arising from the boost to a frame in which the total momentum of the interacting pair is non-vanishing. These corrections are necessary to use phenomenological potentials, describing interactions between nucleons in their center of mass frame, in a locally inertial frame associated with the star. The maximum mass for this EOS is  $M_{max} = 2.20 M_\odot$ .

The matter composition of BBS1 is the same as in the APR2 model. The EOS is obtained using a slightly

different Hamiltonian, including the Argonne  $v_{18}$  two-nucleon potential and the Urbana VII three-nucleon potential [31]. The ground state energy is calculated using G-matrix perturbation theory [32]. The maximum mass is  $M_{max} = 2.01 M_\odot$ .

As representative of the RMFT approach, we choose the EOSs named BGN1H1, GNH3 and BPAL.

The Balberg-Gal (BGN1H1) EOS [33] describes matter consisting of neutrons, protons, electrons, muons and hyperons ( $\Sigma, \Lambda$  and  $\Xi$ ) in equilibrium. The effective potential parameters are tuned in order to reproduce the properties of nuclei and hypernuclei according to high energy experiments. This EOS is a generalization of the Lattimer-Swesty EOS [34], which does not include hyperons. The maximum mass is  $M_{max} = 1.63 M_\odot$ .

The Glendenning (GNH3) EOS [35] considers  $n, p, e, \mu$  up to a certain density  $\rho_H \simeq 2\rho_0$ ; beyond this point, additional baryon states (such as the  $\Delta$  and the hyperons  $\Lambda, \Sigma, \Xi$ ) and the mesons  $\pi, \sigma, \rho, \omega, K, K^*$  are introduced. Below the hadronization density  $\rho_H$  the EOS is very stiff but causal; the appearance of hyperons strongly softens the EOS because they are more massive than nucleons and when they start to fill their Fermi sea they are slow and replace the highest energy nucleons. The maximum mass is  $M_{max} = 1.96 M_\odot$ .

The three EOSs BPAL12, BPAL22 and BPAL32, are derived using a density dependent nucleon-nucleon effective interaction (as for Skyrme nuclear interactions) [36]. Matter is composed of  $n, p, e, \mu$  in weak equilibrium, no hyperons are present and the EOS parameters are fixed to reproduce the saturation properties of nuclear matter. BPAL12 is particularly soft, with a nuclear incompressibility  $k = 120$  MeV. Since the empirical value commonly accepted ranges within  $k \in (220 - 270)$  MeV, it is clear that BPAL12 has to be considered as an EOS soft extreme, but still compatible with astrophysical observations, since the maximum mass it predicts is  $M_{max} = 1.45 M_\odot$ . BPAL22 and BPAL32 are two different versions of the BPAL EOS, corresponding to more realistic values of  $k$ :  $k = 180$  MeV for BPAL22, with a maximum mass  $M_{max} = 1.72 M_\odot$ , and  $k = 240$  MeV for BPAL32, with a maximum mass  $M_{max} = 1.93 M_\odot$ . At a density of about one half of the nuclear saturation density we match the EOS of the core with a crust, which is composed of three layers; the inner layer is the Douchin-Haensel (SLy4) crust [37, 38]; for  $10^8 < \rho < 10^{11}$  g/cm<sup>3</sup> and for  $\rho < 10^8$  g/cm<sup>3</sup>, we use, respectively the Haensel-Pichon (HP94) EOS [39], and the Baym-Pethick-Sutherland (BPS) EOS [40].

In Fig. 1 we show the mass-radius diagram for the selected EOSs. They clearly exhibit very different behaviours. To some extent, BPAL12 and GNH3 can be considered, respectively, as soft and hard extremes. APR2 has a wide mass interval where the radius is almost insensitive to mass variations; BGN1H1 also shows this feature, albeit for a more restricted mass interval, whereas the BPAL and GNH3 EOSs do not. BGN1H1, on the other hand, has a sudden softening which does

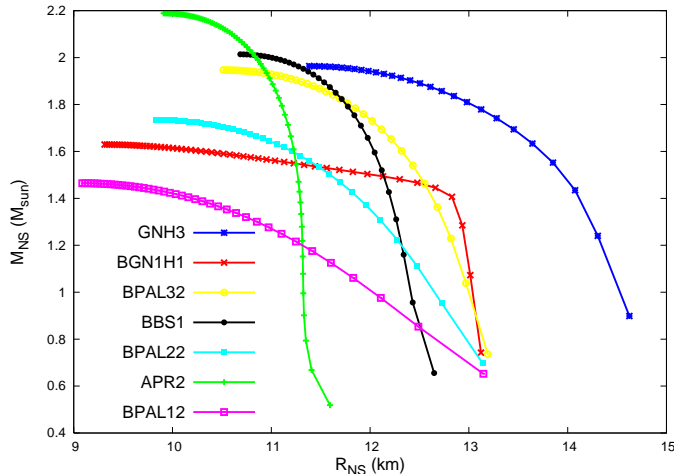


FIG. 1: (Color online) The neutron star mass is plotted versus the stellar radius for the EOSs used in this paper.

not characterise the other three equations of state; this softening is due to the appearance of hyperons in the core of the neutron star above a critical central density.

## V. ERROR BAR ON $R_{NS}$ AND ON $\nu_{GWtide}$

Let us suppose that in a BH-NS coalescence the neutron star is disrupted before reaching the ISCO, and that the gravitational wave interferometers detect the emitted signal which, as discussed in previous sections, has the form of a chirp truncated at the frequency  $\nu_{GWtide}$ . With a suitable data analysis, the values of the symmetric mass ratio  $\eta = M_{BH}M_{NS}/(M_{BH} + M_{NS})^2$  and of the chirp mass  $\mathcal{M} = \eta^{3/5}(M_{BH} + M_{NS})$  can be extracted from the data with a certain error. These errors have been evaluated for non-spinning compact binary sources, including up to 3.5PN terms, in [41],[42]. For instance, they are displayed in Fig. 12 of [42], which shows the one-sigma fractional errors in  $\mathcal{M}$  and  $\eta$  for non-spinning binary black hole sources as a function of the total mass of the system. These errors reduce when the dynamical evolution of spins is included, so that they may be regarded as upper limits. Since a similar analysis has not been performed in the BH-NS case, in what follows we shall adopt these errors as appropriate also for mixed binaries. In the following we shall consider neutron stars whose mass is in the range 1.2 – 1.6 solar masses and mass ratios from 3 to 15, therefore the total mass will range within  $\sim 5 - 26 M_{\odot}$ . In this region the fractional error on  $\mathcal{M}$  is smaller than  $\sim 10^{-3}$  and of the order of  $\sim 1 - 3 \cdot 10^{-2}$  for  $\eta$ . These data refer to advanced LIGO assuming the source at a fixed distance of 300 Mpc.

Since in our case the mass parameters of the binary are the neutron star mass and the mass ratio, we express

TABLE I: Absolute errors on the neutron star mass and on the mass ratio.  $\Delta q$  is independent of the neutron star mass.  $\Delta M_{NS}$  is expressed in solar mass units.

		$1.2 M_{\odot}$	$1.4 M_{\odot}$	$1.6 M_{\odot}$
$q$	$\Delta q$	$\Delta M_{NS}$	$\Delta M_{NS}$	$\Delta M_{NS}$
3	0.12	0.02	0.03	0.03
5	0.15	0.017	0.02	0.02
10	0.24	0.013	0.015	0.018
15	0.34	0.012	0.015	0.017

$\mathcal{M}$  and  $\eta$  as

$$\eta = \frac{q}{(1+q)^2}, \quad \mathcal{M} = \frac{M_{NS}q^{3/5}}{(1+q)^{1/5}}. \quad (36)$$

By propagating the errors we find the following expressions for the one-sigma fractional errors in the neutron star mass and in the mass ratio:

$$\frac{\Delta q}{q} = \frac{q+1}{q-1} \frac{\Delta \eta}{\eta} \quad (37)$$

$$\frac{\Delta M_{NS}}{M_{NS}} = \frac{\Delta \mathcal{M}}{\mathcal{M}} + \frac{2q+3}{5(q-1)} \frac{\Delta \eta}{\eta}. \quad (38)$$

The absolute error on  $M_{NS}$  and  $q$  for the binaries we consider are given in Table I. We shall now discuss how the errors which affect the estimate of the binary parameters influence the evaluation of the neutron star radius and of  $\nu_{GWtide}$ . Since we do not know the error on the black hole angular momentum, in what follows we shall assume that, with an accurate post-detection data analysis,  $a/M_{BH}$  could be measured with a 10% accuracy. As an example, let us suppose that the neutron star mass and the mass ratio measured from a detected signal are, say,  $1.4 M_{\odot}$  and 5, respectively, plus or minus the corresponding error which can be found in Table I. In Fig. 2 we plot the neutron star radius versus  $\nu_{GWtide}$ , evaluated as explained in section III, for any possible combination of the following data:

$$M_{NS} = (1.4 \pm 0.02) M_{\odot}, \quad \frac{a}{M_{BH}} = 0.5 \pm 0.05, \quad q = 5 \pm 0.15, \quad (39)$$

and for a given EOS, for instance BPAL12.

The data are spread in a region which can be identified by a vertical and a horizontal error bar, indicated as a red cross in the figure: the vertical error corresponds to the maximum and minimum values of the neutron star mass. The horizontal error is identified by the points  $(M_{NS} - \Delta M_{NS}, q + \Delta q, a_{min})$  and  $(M_{NS} + \Delta M_{NS}, q - \Delta q, a_{max})$ . In the following figures, where we will show the graphs of  $R_{NS}$  versus  $\nu_{GWtide}$  for different values of the binary parameters and for different EOSs, we shall plot directly the cross, determined as in Fig. 2.

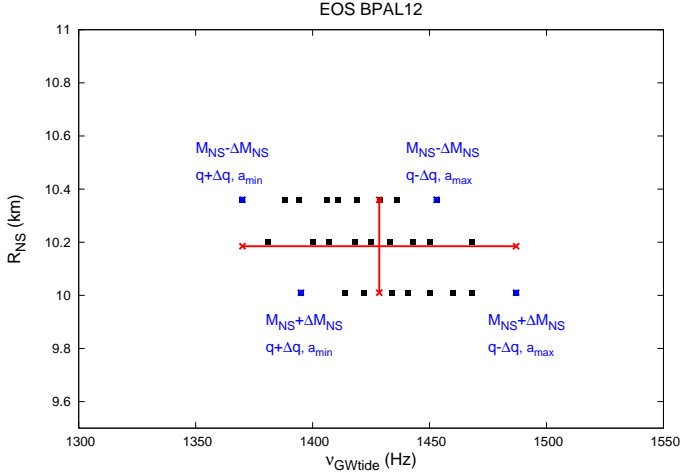


FIG. 2: (Color online) The NS radius is plotted versus  $\nu_{GWtide}$  for any possible combination of the following data:  $M_{NS} = 1.4 \pm 0.02 M_{\odot}$ ,  $a/M_{BH} = 0.5 \pm 0.05$ ,  $q = 5 \pm 0.15$ , and for the EOS BPAL12. The horizontal and vertical spread of the data identify the error bars (red cross).

## VI. RESULTS

The results of our calculations are summarised in the Figs. 3-9.

In Fig. 3 we plot the NS radius,  $R_{NS}$ , versus the cutoff frequency,  $\nu_{GWtide}$ , for a black hole with angular momentum  $a/M_{BH} = 0.9 \pm 0.09$ , and for a neutron star with mass  $M_{NS} = 1.4 M_{\odot} \pm \Delta M_{NS}$  in Fig. 3(a), and  $M_{NS} = 1.2 M_{\odot} \pm \Delta M_{NS}$  in Fig. 3(b). The data are plotted for different values of the mass ratio  $q \pm \Delta q$  (we omit writing “ $\pm \Delta q$ ” in the figures) and for the considered EOSs. The values of  $\Delta M_{NS}$  and  $\Delta q$  are given in Table I. For each value of  $q$ , the continuous black lines are parabolic fits of the data corresponding to each EOS. Fig. 3 shows that, for a given EOS, as  $q$  increases  $\nu_{GWtide}$  decreases. Moreover, for  $q = 15$  the data corresponding to the EOSs BBS1, BPAL22, APR2, BPAL12 are missing. This behaviour is easily understood if we plot the radius at which disruption occurs,  $r_{tide}$ , versus  $\nu_{GWtide}$  for different values of  $q$ . For instance, in Fig. 4 this plot is done for  $M_{NS} = 1.4 M_{\odot}$  and  $a/M_{BH} = 0.9$  for the EOSs BGN1H1 and BPAL12. For comparison, we also plot the value of  $r_{ISCO}$ , given by Eqs. (18), versus the frequency  $\nu_{GW ISCO}$  of the gravitational signal emitted when a point mass of mass  $M = M_{NS}$ , orbiting around a Kerr black hole of mass  $M_{BH} = qM$  and angular momentum  $a/M_{BH} = 0.9$ , reaches  $r_{ISCO}$ . For the BGN1H1 star (upper curve) we see that  $r_{tide}$  is larger than  $r_{ISCO}$  for all values of  $q$ ; thus the GW signal emitted by these systems will exhibit a frequency cutoff at  $\nu_{GWtide}$ . Moreover, as  $q$  increases the value of  $r_{tide}$  increases, i.e. the star is disrupted at larger distances from the black hole. As a consequence  $\nu_{GWtide}$  is a decreasing function of  $q$ ,

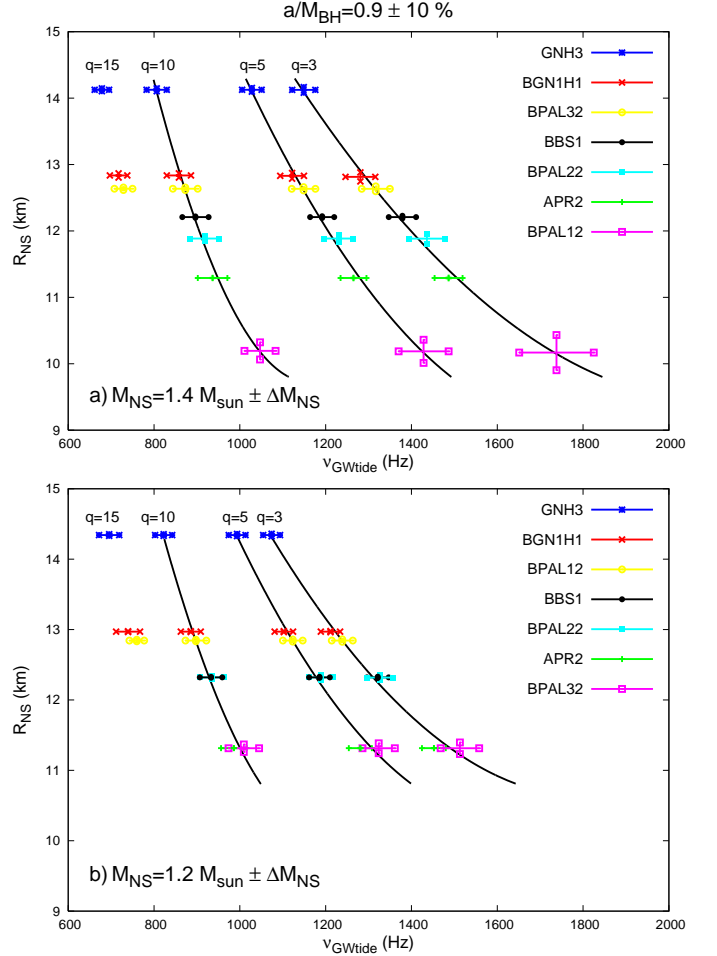


FIG. 3: (Color online)  $R_{NS}$  is plotted versus  $\nu_{GWtide}$ , for a black hole with angular momentum  $a/M_{BH} = 0.9 \pm 0.09$  and a neutron star with mass  $M_{NS} = 1.4 M_{\odot} \pm \Delta M_{NS}$  (upper panel) and  $M_{NS} = 1.2 M_{\odot} \pm \Delta M_{NS}$  (lower panel). The data are plotted for different values of the mass ratio  $q \pm \Delta q$  and for the EOSs considered in section IV. The values of  $\Delta M_{NS}$  and  $\Delta q$  are given in Table I. Black continuous lines are the parabolic fits of the data corresponding to each EOS at fixed  $q$ .

as shown in Fig. 3 for all EOSs.

A similar behaviour is shown by the EOS BPAL12 (middle curve) up to  $q = 10$ . At that point the curve  $r_{tide}$ -versus- $\nu_{GWtide}$  crosses the lower curve  $r_{ISCO}$ -versus- $\nu_{GW ISCO}$ , and for larger  $q$   $r_{tide}$  becomes smaller than  $r_{ISCO}$ ; this means that, for  $q > 10$ , the BPAL12 star would be disrupted after reaching the ISCO and the emitted signal would not exhibit a frequency cutoff. For this reason the part of curve between the points corresponding to  $q = 10$  and  $q = 15$  is indicated as a dashed line. Going back to Fig. 3, the above discussion clarifies why for  $q = 15$  the data for the EOSs BBS1, BPAL22, APR2 and BPAL12 are missing: the star merges with the black hole without being disrupted, and there is no frequency

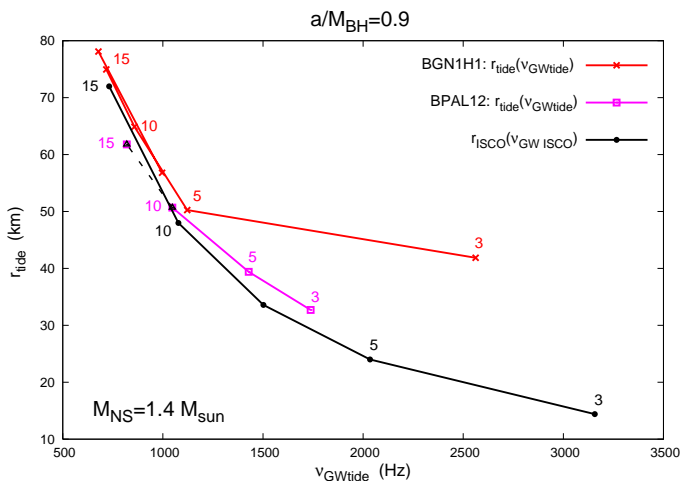


FIG. 4: (Color online) The tidal disruption radius,  $r_{\text{tide}}$ , is plotted versus  $\nu_{\text{GW} \text{tide}}$  for the EOSs BGN1H1 (upper curve) and BPAL12 (middle curve), assuming  $M_{\text{NS}} = 1.4 M_{\odot}$  and  $a/M_{\text{BH}} = 0.9$ . The numbers label points corresponding to different values of  $q$ . For the same values of  $q$  we also plot the value of  $r_{\text{ISCO}}$  (lower curve) versus the corresponding frequency  $\nu_{\text{GW} \text{ISCO}}$  (see text). The dashed part of the curve for BPAL12 refers to values of  $q$  for which the star is not disrupted before the ISCO, i.e. for which  $r_{\text{tide}} < r_{\text{ISCO}}$ .

cutoff in the emitted GW signal.

In Fig. 3 we also notice that the vertical errors are always much smaller than the horizontal ones, except for the EOS BPAL12, when  $M_{\text{NS}} = 1.4 M_{\odot} \pm \Delta M_{\text{NS}}$ . The reason is that the vertical error is due to the error on the neutron star mass, which we recall is of the order of a few percent; the curves corresponding to the different EOSs in the mass-radius diagram of Fig. 1 show that, for  $M_{\text{NS}} = 1.4 M_{\odot}$  or  $M_{\text{NS}} = 1.2 M_{\odot}$ , the stellar radius does not change significantly for such a small change in  $M_{\text{NS}}$ . However,  $M_{\text{NS}} = 1.4 M_{\odot}$  is close to the maximum mass of the BPAL12 EOS, and in its neighborhood the mass-radius curve is almost flat. For this EOS even a small change in the mass corresponds to a significant change in the radius.

Fig. 3(b) shows that, when  $M_{\text{NS}} = 1.2 M_{\odot} \pm \Delta M_{\text{NS}}$ , for the pairs of EOSs (BBS1, BPAL22) and (APR2, BPAL12) the data nearly coincide. The reason is that, as shown in Fig. 1, for  $M_{\text{NS}} = 1.2 M_{\odot}$  the stars corresponding to these pairs of EOSs have nearly the same radius. For the same reason the values of  $\nu_{\text{GW} \text{tide}}$  for BGN1H1 and BPAL32 are very close.

In Fig. 5 the same quantities of Fig. 3 are plotted for a larger mass,  $M_{\text{NS}} = 1.6 M_{\odot} \pm \Delta M_{\text{NS}}$ . The data for the EOS BPAL12 are missing because the maximum mass allowed by this EOS is  $M_{\text{max}} = 1.45 M_{\odot}$ . A comparison with Fig. 3(a) shows that, for  $M_{\text{NS}} = 1.6 M_{\odot}$ , the data for the EOS BGN1H1 move at the bottom of the figure, i.e. for these masses the NS radius is smaller than that given by the other EOSs, as can also be seen from

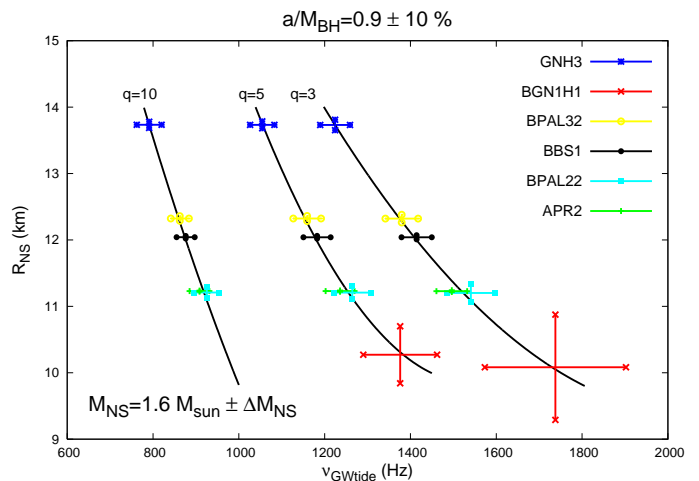


FIG. 5: (Color online) The same plot as in Fig. 3, but for  $M_{\text{NS}} = 1.6 M_{\odot} \pm \Delta M_{\text{NS}}$ .

Fig. 1; moreover, the vertical error bars are larger, because for this EOS  $M_{\text{NS}} = 1.6 M_{\odot}$  is very close to the maximum mass, where the mass-radius curve is nearly flat (see Fig. 1).

In Fig. 6 the same quantities of Fig. 3 are plotted for a black hole with angular momentum  $a/M_{\text{BH}} = 0.5 \pm 0.05$ . Fig. 6(a) refers to a neutron star with mass  $M_{\text{NS}} = 1.4 M_{\odot} \pm \Delta M_{\text{NS}}$ , whereas in Fig. 6(b)  $M_{\text{NS}} = 1.2 M_{\odot} \pm \Delta M_{\text{NS}}$ . The data for  $q = 10$  and 15 are missing because no disruption occurs for the considered EOS: tidal disruption is favoured by large values of the black hole angular momentum.

If we compare this figure with Fig. 3 we see that, for a given mass and EOS, the value of the cutoff frequency is smaller if the black hole angular momentum decreases. This means that the tidal disruption radius  $r_{\text{tide}}$  increases as  $a$  decreases. It should be noted that for a fixed value of  $M_{\text{NS}}$  and of  $q$   $r_{\text{ISCO}}$  also increases as  $a$  decreases; it increases faster than  $r_{\text{tide}}$ , therefore there exists a critical value of the black hole angular momentum *below* which the star is not disrupted before the ISCO. In a similar way, for fixed  $a$ ,  $M_{\text{NS}}$  and EOS, there exists a critical value of  $q$  *above* which no disruption occurs. As an example, in Table II we give the values of  $q_{\text{max}}$  and the corresponding  $\nu_{\text{GW} \text{tide}}$ , which is the minimum value of the cutoff frequency to be expected, for the binaries considered in Figs. 3 and 6.

A direct comparison of the effect of the angular momentum on  $\nu_{\text{GW} \text{tide}}$  is displayed in Fig. 7 where the plot of  $R_{\text{NS}}$  versus  $\nu_{\text{GW} \text{tide}}$  is done for  $M_{\text{NS}} = 1.4 M_{\odot} \pm \Delta M_{\text{NS}}$ ,  $q = 3 \pm \Delta q$  and for  $a/M_{\text{BH}} = 0.9 \pm 10\%$  and  $0.5 \pm 10\%$ . We see that the effect is small, but not negligible.



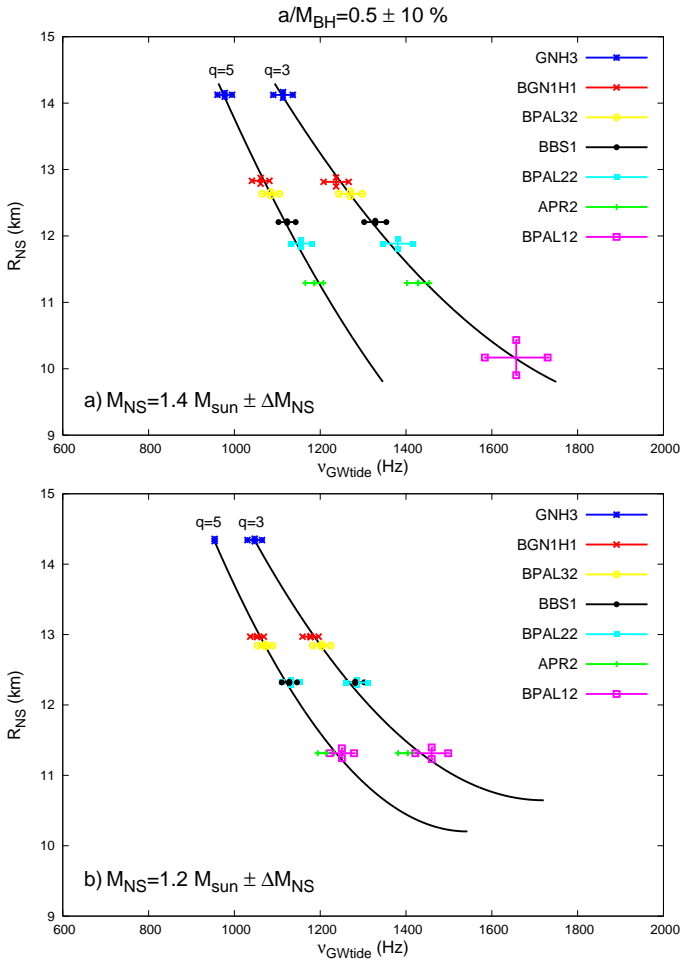


FIG. 6: (Color online) The same plot as in Fig. 3 for a black hole with angular momentum  $a/M_{BH} = 0.5 \pm 0.05$ . The data for  $q = 10$  and  $15$  are missing because no disruption occurs for the considered EOSs.

An interesting feature common to the Figs. 3, 5 and 6 is that, for the considered EOSs, all data are well fitted by a parabolic fit.

It should be noted that the fit proposed by Vallisneri in ref. [13], i.e.

$$\frac{R_{NS}}{M_{NS}^{1/3} M_{BH}^{2/3}} \approx \begin{cases} 0.145(\tilde{\nu} M_{BH})^{-0.71} & \text{for } \tilde{\nu} M_{BH} \lesssim 0.045 \\ 0.069(\tilde{\nu} M_{BH})^{-0.95} & \text{for } \tilde{\nu} M_{BH} \gtrsim 0.045 \end{cases} \quad (40)$$

(where  $\tilde{\nu} \equiv \nu_{GWtide}$ ) for  $M_{NS} = 1.4 M_{\odot}$  and  $M_{BH} = (2.5-80) M_{\odot}$ , predicts values of  $R_{NS}$  and  $\nu_{GWtide}$  largely different from those we find, as shown in Fig. 8. In particular we see that, for a given value of the NS mass, of the radius (i.e. of the stellar compactness) and of the mass ratio, the value of  $\nu_{GWtide}$  evaluated in [13] is systematically smaller than the value we find. This happens for a number of reasons. For instance, let us consider two binary systems having a black hole of the

TABLE II: The values of  $q$  above which no disruption occurs,  $q_{max}$ , and the corresponding minimum value of  $\nu_{GWtide}$ ,  $\nu_{min}$ , are tabulated for the binaries considered in Figs. 3 and 6, i.e. for a black hole with  $a/M_{BH} = 0.5, 0.9$  and a neutron star with mass  $M = 1.2, 1.4 M_{\odot}$ .

$a/M_{BH} = 0.5$				
EOS	$1.2 M_{\odot}$		$1.4 M_{\odot}$	
	$q_{max}$	$\nu_{min}$ (Hz)	$q_{max}$	$\nu_{min}$ (Hz)
GNH3	9.4	780	7.5	840
BGN1H1	8.4	878	6.7	942
BPAL32	8.2	899	6.6	967
BBS1	7.6	966	6.1	1032
BPAL22	7.6	968	5.8	1084
APR2	6.9	1068	5.6	1128
BPAL12	6.6	1116	4.6	1375
$a/M_{BH} = 0.9$				
GNH3	23.2	559	18.5	596
BGN1H1	20.6	628	16.5	667
BPAL32	20.1	642	15.9	690
BBS1	18.8	686	15.1	726
BPAL22	18.9	689	14.4	759
APR2	17.0	757	13.8	793
BPAL12	16.2	790	11.3	960

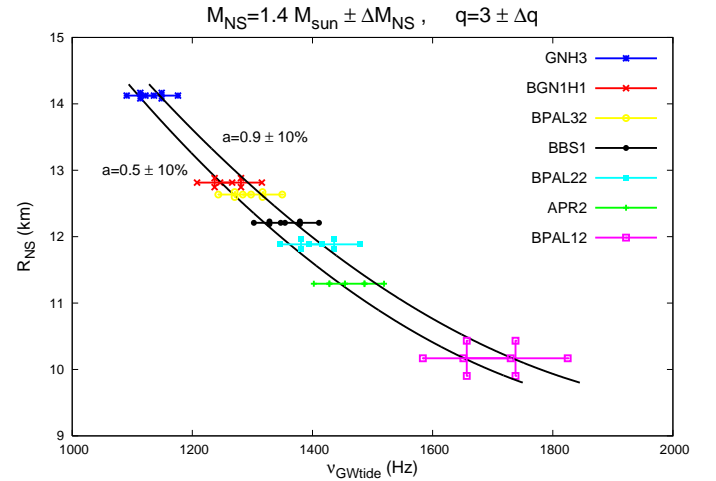


FIG. 7: (Color online) The plot of  $R_{NS}$  versus  $\nu_{GWtide}$  is done for the same NS mass,  $M_{NS} = 1.4 M_{\odot} \pm \Delta M_{NS}$ , the same mass ratio  $q = 3 \pm \Delta q$ , and two different values of the angular momentum,  $a = 0.9 \pm 10\%$  and  $a = 0.5 \pm 10\%$ .

same mass and a neutron star with the same mass and compactness; in one case the NS structure is computed using the equations of Newtonian gravity and an  $n = 1$  polytropic EOS, in the other case using the TOV equations and one of the EOS we consider in this paper. If we evaluate the value of  $r_{tide}$  for the first system using the affine approach in Newtonian gravity as in [13], and for the second system using our improved affine approach,

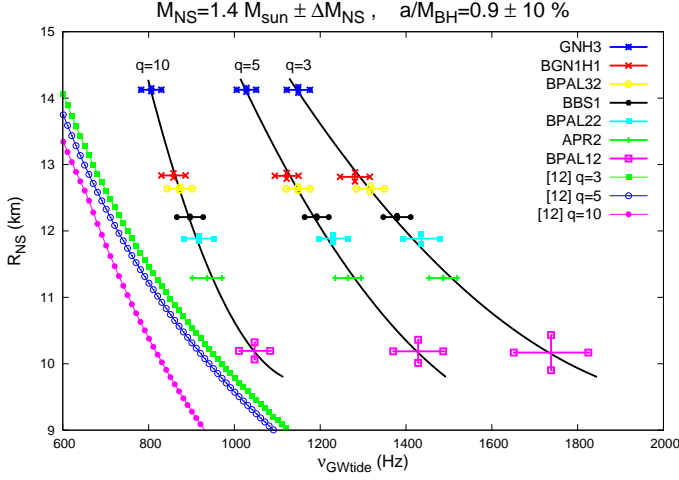


FIG. 8: (Color online) The data of Fig. 3 are compared to the fit given in Eq. 40 [13].

TABLE III: The parameters  $\alpha, \beta, \gamma$  of our parabolic fits.  $\alpha$  is in km,  $\beta$  in km/Hz,  $\gamma$  in km/Hz<sup>2</sup>.

$a/M_{BH} = 0.5$						
	$1.2 M_{\odot}$			$1.4 M_{\odot}$		
$q$	$\alpha$	$\beta$	$\gamma$	$\alpha$	$\beta$	$\gamma$
3	34.7	$-2.8 \cdot 10^{-2}$	$8.1 \cdot 10^{-6}$	32.4	$-2.3 \cdot 10^{-2}$	$5.5 \cdot 10^{-6}$
5	38.5	$-3.6 \cdot 10^{-2}$	$11.9 \cdot 10^{-6}$	35.3	$-2.9 \cdot 10^{-2}$	$7.5 \cdot 10^{-6}$
$a/M_{BH} = 0.9$						
3	33.2	$-2.5 \cdot 10^{-2}$	$6.9 \cdot 10^{-6}$	31.7	$-2.1 \cdot 10^{-2}$	$5.0 \cdot 10^{-6}$
5	37.1	$-3.3 \cdot 10^{-2}$	$10.2 \cdot 10^{-6}$	37.4	$-3.2 \cdot 10^{-2}$	$9.0 \cdot 10^{-6}$
10	50.0	$-6.7 \cdot 10^{-2}$	$27.7 \cdot 10^{-6}$	56.3	$-8.0 \cdot 10^{-2}$	$34.5 \cdot 10^{-6}$
15	47.9	$-7.1 \cdot 10^{-2}$	$32.4 \cdot 10^{-6}$	189.8	-0.47	$31.4 \cdot 10^{-5}$

we will always find  $r_{tide}^{Newtonian} > r_{tide}^{improved}$ . As a consequence the value of  $\nu_{GWtide}$  evaluated by the Newtonian approach will be smaller than that evaluated with our improved approach. Furthermore, given the value of  $r_{tide}$ , in [13]  $\nu_{GWtide}$  is calculated using the formula for a point mass moving on a circular orbit in Kerr space-time, while we compute this quantity using the 2.5 Post Newtonian equations describing the orbital evolution of a binary system. This introduces a further difference which makes our  $\nu_{GWtide}$  larger than that evaluated with the geodesic approximation, and the difference increases when we consider small values of the mass ratio  $q$ , as shown in Fig. 8.

The parameters  $\alpha, \beta, \gamma$  of our parabolic fits

$$R_{NS} = \alpha + \beta \nu_{GWtide} + \gamma \nu_{GWtide}^2, \quad (41)$$

where  $R_{NS}$  is expressed in km and  $\nu_{GWtide}$  in Hz, are given in Table III.

We shall now discuss how the results of this paper could be used to estimate the radius of the star and to gain information on the equation of state, using gravitational wave detection.

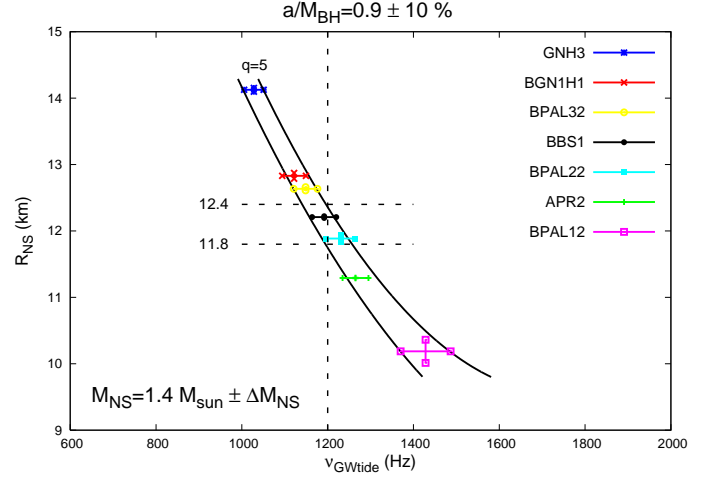


FIG. 9: (Color online)  $R_{NS}$  versus  $\nu_{GWtide}$  is plotted for  $M_{NS} = 1.4 M_{\odot} \pm \Delta M_{NS}$ ,  $q = 5 \pm \Delta q$  and  $a/M_{BH} = 0.9 \pm 0.09$ . The black continuous lines are the parabolic fits of the extreme points of the horizontal error bar for each EOS. The vertical dashed line corresponds to the supposed detected value of  $\nu_{GWtide}$ . The two horizontal dashed lines identify the uncertainty on the evaluation of  $R_{NS}$ .

Let us assume that a gravitational wave signal has been detected and exhibits a frequency cutoff at, say,  $\nu_{GWtide} = 1200$  Hz. A suitable data analysis on the chirp part of the signal allows to determine the neutron star mass, the mass ratio, with the corresponding uncertainty given in Table I, and the black hole angular momentum with, say, an error of about 10%. Let us suppose that their values are  $M_{NS} = 1.4 M_{\odot} \pm \Delta M_{NS}$ ,  $q = 5 \pm \Delta q$  and  $a/M_{BH} = 0.9 \pm 0.09$ , with  $\Delta M_{NS}$  and  $\Delta q$  given in Table I. With this information, we compute the NS radius versus  $\nu_{GWtide}$  for the considered EOSs as explained in section II 2, and plot the results in Fig. 9. The two continuous black lines are the parabolic fits of the points which, for each EOS, are at the extreme of the horizontal error bar. If we draw a vertical line corresponding to the supposed detected cutoff frequency, i.e.  $\nu_{GWtide} = 1200$  Hz, we see that it intercepts the two lines in two points, which identify a region within which the stellar radius should fall. The data shown in Fig. 9 tell us that we would determine the NS radius with an error of 2.5%. The error would be smaller if the detected value of  $\nu_{GWtide}$  is smaller, and larger if it is larger. For instance for  $\nu_{GWtide} = 1400$  Hz it would be 3.3%, and 2.2% for  $\nu_{GWtide} = 1100$  Hz.

Moreover, we would be able to exclude the EOSs which fall outside the region framed by the horizontal dashed lines, putting strict constraints on the equation of state inside the neutron star.

## VII. CONCLUDING REMARKS

In this paper we show that, by detecting a gravitational wave signal emitted by a BH-NS coalescing binary which exhibits a frequency cutoff due to the disruption of the star before the ISCO, we may be able to determine the radius of the star with quite a good accuracy, of the order of a few percent, and to put strict constraints on the equation of state of matter in the neutron star core.

Our study does not intend to be exhaustive, since many more equations of state may be considered in the analysis; for instance we did not consider quark stars. There may exist other branches in the plots shown in Figs. 3-7 corresponding to more exotic EOSs.

However, from our study it emerges that the quantity which mostly affects  $\nu_{GWtide}$  is the stellar compactness; therefore, we expect that in general the cutoff frequencies lay on the parabolic fits which correspond to a given neutron star mass, mass ratio and black hole angular momentum.

A further point which should be discussed is the following. In our analysis we have assumed that the value of  $\nu_{GWtide}$  is known from the detection of a gravitational wave signal, but of course this quantity also is affected by

uncertainties. For instance, we do not know how quickly the amplitude of the chirp goes to zero at tidal disruption, and therefore how sharp the step in the Fourier transform of the gravitational signal  $h(\nu)$  at  $\nu_{GWtide}$  is. To answer this question, an accurate modeling of the BH-NS coalescence process is certainly needed. Moreover, assuming a given “slope” in  $h(\nu)$  at tidal disruption, how large would the experimental error in the determination of  $\nu_{GWtide}$  be? We plan to investigate this problem with a suitable data analysis study on the data of Virgo.

## Acknowledgements

We are indebted to Ignazio Bombaci for kindly providing the data for the EOSs BPAL12, 22 and 32, and to Omar Benhar for useful suggestions and discussions.

This work was partially supported by CompStar, a research networking program of the European Science Foundation. L.G. has been partially supported by Grant No. PTDC/FIS/098025/2008. F.P. was supported in part by DFG Grant SFB/Transergio7 ”Gravitational Wave Astronomy”.

- 
- [1] <http://www.ego-gw.it>; <http://ligo.caltech.edu>.  
 [2] <http://www.et-gw.eu>.  
 [3] A. Sadowski, K. Belczynski, T. Bulik, N. Ivanova, F.A. Rasio and R. O’Shaughnessy, *Astrophys. J.* **676**, 1162, (2008).  
 [4] B. Carter, J.P. Luminet, *Mon. Not. R. Astron. Soc.* **212**, 23, (1985).  
 [5] J.P. Luminet, J.A. Marck, *Mon. Not. R. Astron. Soc.* **212**, 57, (1985).  
 [6] P. Wiggins, D. Lai, *Astrophys. J.* **532**, 530, (2000).  
 [7] J.M. Lattimer, D.N. Schramm, *Astrophys. J.* **210**, 549 (1976).  
 [8] V. Ferrari, L. Gualtieri, F. Pannarale, *Class. Quant. Grav.* **26** 125004, (2009).  
 [9] W. H. Lee, W. Kluzniak, *Mon. Not. R. Astron. Soc.* **308**, 780, (1999).  
 [10] W. H. Lee, *Mon. Not. R. Astron. Soc.* **328**, 583, (2001).  
 [11] Z. B. Etienne, Y. T. Liu, S. L. Shapiro, T. W. Baumgarte, *Phys. Rev. D* **79**, 044024 (2009).  
 [12] E. Rantsiou, S. Kobayashi, P. Laguna, F. A. Rasio, *Astrophys. J.* **680**, 1326, (2008).  
 [13] M. Vallisneri, *Phys. Rev. Lett.* **84**, 3519 (2000).  
 [14] M. Shibata, *Prog. Theor. Phys.* **96**, 917 (1996).  
 [15] J. A. Faber, *Class. Quant. Grav.* **26**, 114004, (2009).  
 [16] J. A. Faber, T. W. Baumgarte, S. L. Shapiro, K. Taniguchi, F. A. Rasio, *Phys. Rev. D* **73**, 024012 (2006).  
 [17] J. A. Faber, T. W. Baumgarte, S. L. Shapiro, K. Taniguchi, *Astrophys. J.* **641**, L93, (2006).  
 [18] M. Shibata, K. Uryu, *Class. Quant. Grav.* **24**, S125, (2007).  
 [19] K. Taniguchi, T. W. Baumgarte, J. A. Faber, S. L. Shapiro, *Phys. Rev. D* **75**, 084005, (2007).  
 [20] S. Chandrasekhar *Ellipsoidal Figures of Equilibrium* (The Silliman Foundation Lectures, New Haven: Yale University Press), (1969).  
 [21] J.-A. Marck *Proc. Roy. Soc. Lond. A*, **385**, 431, (1983).  
 [22] W. H. Press, S. A. Teukolsky, W. T. Vetterling, and B. P. Flannery, *Numerical recipes in FORTRAN. The art of scientific computing* (Cambridge University Press, 1992).  
 [23] J.M. Lattimer, M. Prakash, *Phys. Rep.* **442**, 109, (2007).  
 [24] J. M. Bardeen, W. H. Press, S. A. Teukolsky, *Astrophys. J.* **178**, 347, (1972).  
 [25] A. Buonanno, Y. Chen, and T. Damour, *Phys. Rev. D* **74**, 104005 (2006).  
 [26] G. Schäfer, *Ann. Phys.* **161**, 81 (1985).  
 [27] R. B. Wiringa, V. G. J. Stoks, R. Schiavilla, *Phys. Rev. C* **51**, 38, (1995).  
 [28] B. S. Pudliner, V. R. Pandharipande, J. Carlson, S. C. Pieper, R. B. Wiringa, *Phys. Rev. C* **56**, 1720, (1997).  
 [29] A. Akmal, V. R. Pandharipande, *Phys. Rev. C* **56**, 2261, (1997).  
 [30] A. Akmal, V. R. Pandharipande, D.G. Ravenhall *Phys. Rev. C* **58**, 1804, (1998).  
 [31] R. Schiavilla, V. R. Pandharipande, R.B. Wiringa, *Nucl. Phys. A* **449**, 219 (1986).  
 [32] M. Baldo, G. F. Burgio, H. J. Schulze, *Phys. Rev. C* **61**, 055801, (2000).  
 [33] S. Balberg, A. Gal, *Nucl. Phys. A* **625**, 435, (1997).  
 [34] J. M. Lattimer, F. D. Swesty, *Nucl. Phys. A* **535**, 331, (1991).  
 [35] N. K. Glendenning, *Astrophys. J.* **293**, 470, (1985).  
 [36] I. Bombaci, in *Perspectives on Theoretical Nuclear Physics*, Editors: I. Bombaci et al., ETS Pisa, 222 (1996);

- M. Prakash, I. Bombaci, M. Prakash, P. J. Ellis, J. M. Lattimer, R. Knorren, *Phys. Rep.* **280**, 1 (1997).
- [37] F. Douchin, P. Haensel, *Phys. Lett. B* **485**, 107 (2000).
- [38] F. Douchin, P. Haensel, *Astron. & Astroph.* **380**, 151 (2001).
- [39] P. Haensel, B. Pichon, *Astron. & Astroph.* **283**, 313 (1994).
- [40] G. Baym, C. Pethick, P. Sutherland, *Astrophys. J.* **170**, 299, (1971).
- [41] K. G. Arun, B. R. Iyer, B. S. Sathyaprakash, P. A. Sundararajan, *Phys. Rev. D* **71**, 084008, (2005).
- [42] B. S. Sathyaprakash, B. F. Schutz, *Living Reviews in Relativity* **12**, 2, (2009).